Plasma Processes and Polymers

PLASMA PROCESSES AND POLYMERS

RESEARCH ARTICLE OPEN ACCESS

Comparison of the Coating Structure of Silicon-Based PECVD Coatings With Varying Organic Content

Jonas Franke[1] | Maciej Oskar Liedke[2] | Andreas Schäfer[3] | Maik Butterling[2] | Ahmed Gamal Attallah[2] | Eric Hirschmann[2] | Andreas Wagner[2] | Rainer Dahlmann[1]

[1]Institute for Plastics Processing (IKV), RWTH Aachen University, Aachen, Germany | [2]Institute of Radiation Physics, Helmholtz-Zentrum Dresden-Rossendorf, Dresden, Germany | [3]Nanoanalytics GmbH, Münster, Germany

Correspondence: Jonas Franke (jonas.franke@ikv.rwth-aachen.de)

Received: 6 October 2025 | **Revised:** 27 November 2025 | **Accepted:** 1 December 2025

Funding: Deutsche Forschungsgemeinschaft

Keywords: barrier | PECVD | porosity | silicon organic | silicon oxide | structure | transition

ABSTRACT

This study examines the structural transition between plasma-polymerized silicon-oxide (SiO_x) and silicon-organic (SiOCH) coatings with varying organic content. Using comprehensive characterization techniques on 13 samples with systematically varied oxygen-to-hexamethyldisiloxane ratios and energy densities, we found that SiO_x barrier coatings unexpectedly exhibited higher porosity than SiOCH coatings. This suggests chemical composition impacts barrier performance more than nanopore structure. The transition from SiOCH to SiO_x involves molecular-level structural reorganization, likely due to absent Si-C bonds in SiO_x coatings, creating a more rigid SiO_2-like cage structure. These findings provide crucial insights into structure-property relationships of silicon-based plasma coatings, essential for optimizing gas barrier functionality in applications like food packaging.

1 | Introduction

Silicon-based plasma-enhanced chemical vapor deposition (PECVD) coatings represent a rapidly advancing field with superior barrier performance over traditional packaging materials while enabling sustainable, recyclable packaging solutions [1, 2]. Recent breakthroughs demonstrate that optimized SiO_x coatings achieve water vapor transmission rates below 10^{-5} g/m^2/day and withstand 10 000 bending cycles [3], making them ideal for next-generation flexible electronics and food packaging applications. This dynamic is met by estimated cumulative annual growth rates (CAGR) of 10% between 2024 and 2032 of the global market of barrier coatings for the packaging market [4], as well as a CAGR of 9.3% between 2025 and 2032 for the global CVD market [5]. While silicon-based PECVD barrier coatings for the packaging sector represent only a subset of these markets, this underscores the potential of the technology, which has been advanced through extensive research and development, paving the way for high-performance applications.

Among many other process gas combinations, hexamethyldisiloxane (HMDSO) is often used as a precursor with O_2 as an auxiliary gas in PECVD. By varying process parameters such as energy input, gas flows, and pressure, a wide range of properties can be tuned for the coatings. Highly cross-linked, glass-like SiO_x coatings that can act as a gas barrier are deposited by applying a high energy input to dissociate most Si-CH_3 bonds in the HMDSO, while using a high O_2:HMDSO ratio to provide an abundance of oxygen. Due to their good barrier performance, transparency and mechanical stability, SiO_x coatings for a long time have been and still are the subject of many investigations [6–8]. In contrast, HMDSO-based processes with a lower energy input and oxygen supply will result in less cross-linked structures as a result of the incorporation of terminal groups [9]. These silicon oxycarbide (SiOCH) coatings retain significant

amounts of carbon from the original HMDSO precursor, preserving much of the Si-O-Si backbone structure while incorporating methyl groups [10, 11]. The resulting polymer-like films exhibit characteristics similar to polydimethylsiloxane (PDMS), with hydrophobic properties and contact angles reaching up to 110° [11, 12]. While SiOCH coatings generally show inferior barrier performance compared to their inorganic SiO_x counterparts, they serve important functions as adhesion-promoting interlayers between organic substrates and dense barrier films [10, 13]. The flexible, organic nature of SiOCH coatings also makes them suitable for stress relief and can prevent crack formation in multilayer barrier systems during mechanical deformation [13]. Several studies have demonstrated that alternating SiOCH and SiO_x layers in "dyad" structures significantly enhance barrier performance compared to single-layer systems by orders of magnitude [14–16]. Adding to the improved coating adhesion and the internal stress relief, this approach decouples defects in the SiO_x layer, which can be described using the "tortuous-path model" by Nielsen [17].

The synthesis of both SiO_x and SiOCH coatings is already well established, as outlined in the previous paragraph, and their chemical structures have been extensively studied. However, the transition between these two coating types has received comparatively little attention. In an earlier work, the stretch tolerance of different coatings, using a full-factorial experimental design, was examined [18]. Varied parameters were HMDSO and O_2 flow and the microwave pulse-on time. X-ray photoelectron spectroscopy (XPS) and OTR measurements showed that the investigated parameter range contained well-distinguishable SiO_x and SiOCH coatings. Although not the primary focus of this study, no critical parameter or threshold could be identified for the transition between the two coatings. It was evident that within the parameter range, HMDSO flow is one of the decisive factors for the deposition of SiO_x or SiOCH. An increased HMDSO flow was observed for coatings that had a low barrier performance and an increased carbon content, which is typical for SiOCH. In another previous work, this issue was addressed more thoroughly and examined the coating structure of five coatings with varying O_2:HMDSO ratio by means of Doppler broadening variable energy positron annihilation spectroscopy (DB-VEPAS), Water Vapor Transmission Rate (WVTR) and Quartz Crystal Microbalance (QCM) [19]. Again, both SiO_x and SiOCH coatings resulted within the chosen parameter range, where SiO_x resulted from increased O_2:HMDSO ratios. DB-VEPAS is a method to investigate the porous structure of a sample on a nm scale, and is described in the Materials & Methods section. This method revealed that the concentration of open/free volume increases with a decreasing O_2:HMDSO ratio, while the chemical surrounding of an annihilation site shifted from resembling vitreous carbon towards pure SiO_2 with increasing O_2:HMDSO ratio. This suggests a gradual transition of the porous structure from SiOCH to SiO_x. However, no gradual transition can be observed for the permeation properties, but a rather abrupt decline in permeability appears for SiO_x. Nanoscale defects in thin film coatings are, provided that the impact of larger defects such as pinholes is minimized, widely regarded as key determinants of their permeation barrier properties [20, 21]. In that context, note that in the scope of this paper, "pores" refer to nanoscopic, closed defects, and not to pinholes that traverse the entire coating. This understanding implies a strong correlation between a coating's porosity and its barrier performance, suggesting a significant reduction in porosity during the transition from SiOCH to SiO_x. However, the fact that such a drop in porosity could not be observed raises questions about whether other factors may also play a critical role. Previous research [18] identified the C/O ratio as a promising candidate for such a factor.

This work aims to examine this in more detail through a comprehensive structural analysis of different SiOCH and SiO_x coatings. The parameter sets from both earlier works were chosen, as they cover a broad framework within which the transition from SiOCH to SiO_x takes place, resulting in 13 different coatings. For each coating, high-resolution XPS measurements were performed to determine chemical composition and binding states, variable energy positron annihilation lifetime spectroscopy (VEPALS) and DB-VEPAS for extensive characterization of the porosity, and OTR measurements to assess the permeability. This approach aims to gather comprehensive insights on the structure of silicon-based PECVD coatings as a function of their organic content, and their effect on resulting oxygen permeation rates. This knowledge should then be used to test the following hypothesis:

> *The carbon-to-oxygen (C/O) ratio is a critical parameter governing the gas barrier properties of silicon-based PECVD coatings in the range of 30 nm. Rather than exhibiting a continuous relationship where barrier performance gradually improves with decreasing C/O ratio, these coatings demonstrate threshold behavior, transitioning abruptly from low to high barrier efficacy at a specific C/O value.*

2 | Materials and Methods

2.1 | Samples

Coating parameters were taken from earlier works (V1-V8 from [18] and R1-R5 from [19]) and are given in Table 1. All samples were produced on the LAMPS reactor, which is described in detail elsewhere [22]. Only the pulse-on time and both gas flows were varied. These parameters are used to calculate both the O_2:HMDSO ratio and the energy density ε_{plasma} according to Hegemann, with the power input W and gas flows F_i using a HMDSO/O_2 specific correction factor of 0.6 [9]:

$$\varepsilon_{plasma} = \frac{W}{F_{HMDSO} + 0.6{*}F_{O_2}} \quad (1)$$

Plotting these against each other provides an intuitive overview that highlights the key differences between the selected parameter sets. This is done in Figure 1, where parameter sets V1−V8 are displayed as circles, R1−R5 as squares. Depending on whether the coatings exhibited a gas barrier effect, they were marked green (significant barrier, likely SiO_x) or blue (no apparent barrier, likely SiOCH). This encoding is used throughout this paper for all the following figures. In Figure 1, it can be seen that parameter sets V1−V8 and R1 densely screen a small area with $\varepsilon_{plasma} < 15\frac{W}{sccm}$ and O_2:HMDSO < 25. This represents the usual parameter range used for the LAMPS reactor, whereas sets R2−R5 explore its limits in both

TABLE 1 | PECVD coating parameters and calculated values for the O_2:HMDSO ratio and the energy density ε_{plasma}.

	Power [W]	t_{on} [ms]	t_{off} [ms]	O_2 [sccm]	HMDSO [sccm]	Pressure [Pa]	O_2:HMDSO [-]	ε_{plasma} [W/sccm]
V1	4 × 4000	3	45	150	10	5	15	10
V2					30		5	8.3
V3				250	10		25	6.3
V4					30		8.33	5.6
V5		4		150	10		15	13.1
V6					30		5	10.9
V7				250	10		25	8.2
V8					30		8.33	7.3
R1		5		200	20		10	11.4
R2				100			5	20
R3				20			1	50
R4				0			0	80
R5				1000	10		100	2.6

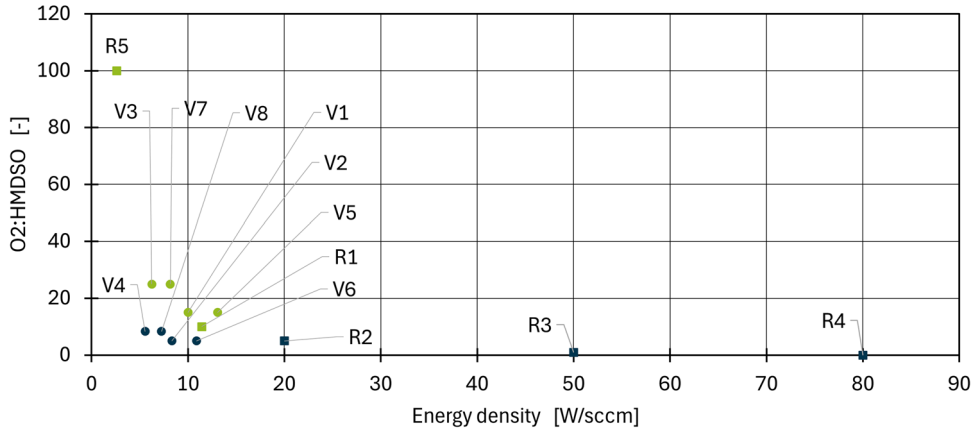

FIGURE 1 | Visual representation of the investigated parameter range.

dimensions. The upper right area of the plot is not covered since this is not possible with the current reactor setup. Also, there seems to be a threshold of the gas ratio between 8.33 and 10, above which the resulting coating will be in the SiO_x domain.

Coating samples for XPS and PAS were applied on silicon wafers with a sputtered 40 nm Au coating in order to get smooth substrates that are clearly different from the applied PECVD coatings, with a coating thickness of ~100 nm. For OTR measurements, coatings were applied on the same 12 µm PET film by Flex Films Inc. as used in the earlier investigations. Here, coating thickness was tuned to ~30 nm to avoid effects such as stress cracking that would have impaired the barrier performance.

2.2 | VEPALS

VEPALS measurements were conducted at the Mono-energetic Positron Source (MePS) beamline at HZDR, Germany [23]. A $CeBr_3$ scintillator detector coupled to a Hamamatsu R13089-100 photomultiplier tube was utilized for gamma photon detection. The signals were processed by the Teledyne SP Devices ADQ14DC-2X digitizer (14-bit vertical resolution and 2GS/s horizontal resolution) [24]. The overall time resolution of the measurement system was ≈0.250 ns, and all spectra contained at least $1{\cdot}10^7$ counts. A typical lifetime spectrum N(t), the absolute value of the time derivative of the positron decay spectrum, is described by

$$N(t) = R(t) * \sum_{i=1}^{k+1} \frac{I_i}{\tau_i} e^{\frac{-t}{\tau_i}} + \text{Background}, \quad (2)$$

where k is the number of different defect types contributing to the positron trapping, which are related to k + 1 components in the spectra with the individual lifetimes τ_i and intensities I_i ($\Sigma I_i = 1$) [25]. The instrument resolution function R(t) is a sum of two Gaussian functions with distinct intensities and a relative shift both depending on the positron implantation energy, E_p. It was determined by the measurement and analysis of a reference sample, that is, Yttria-stabilized zirconia (YSZ), which exhibited a single well-known lifetime component. The background was negligible, hence fixed to zero.

All the spectra were deconvoluted using a non-linear least-squares fitting method, minimized by the Levenberg-Marquardt

algorithm, employed within the fitting software package PALSfit [26] into 5 lifetime components. They directly evidence de- and localized annihilation in point defects as well as para-Positronium (p-Ps) contribution (τ_1), vacancy agglomerations and smallest detected micropores (τ_2), 2 additional micropore types (sizes; τ_3 and τ_4), and ortho-Positronium (o-Ps) from the surface region of the films (τ_5). Their relative intensities scale typically with the concentration of each defect type but are convoluted with each other. In general, positron lifetime increases with defect size and open volume size. The positron lifetime and its intensity have been probed as a function of positron implantation energy $E_{p,}$ which was recalculated to a mean implantation depth, ‹z›. The average positron lifetime τ_{av} is defined as $\tau_{av} = \Sigma_i\ \tau_i \cdot I_i$.

2.3 | DB-VEPAS

DB-VEPAS measurements have been conducted at the apparatus for in-situ defect analysis (AIDA) [27] of the slow positron beamline (SPONSOR) [28] at HZDR, Germany. Positrons have been accelerated and monoenergetically implanted into samples in the range between $E_p = 0.05{-}35$ keV, which allows for depth profiling. A mean positron implantation depth was approximated using a simple material density (ρ) dependent formula [29]:

$$\langle z\rangle\,[\mathrm{nm}] = \frac{36}{\rho\ \ [\mathrm{g{\bullet}cm^{-3}}]} E_p^{1.62}\,[\mathrm{keV}] \tag{3}$$

<z> approximates the depth and cannot be treated as an absolute measure because it does not account for the diffusion of positron and ortho-Positronium (o-Ps). The best estimation it gives for materials with large defect concentration, hence low positron diffusion length. Implanted into a solid, positrons lose their kinetic energy due to thermalization and, after short diffusion, annihilate in delocalized lattice sites or localize in vacancy-like defects and interfaces, emitting usually two anti-collinear 511 keV gamma photons once they meet electrons. At surfaces facing vacuum, for example, in micro- and mesopores, positrons have a chance to convert into a hydrogen-like particle, the so-called Positronium (Ps). The long-living version of Ps the o-Ps can reside in pores for a defined time, depending on the pore size. Since at the annihilation site thermalized positrons and o-Ps have very small momentum compared to the electrons, a broadening of the 511 keV line is observed mostly due to the momentum of the electrons, which is measured with a high-purity Ge detector (energy resolution of 1.09 ± 0.01 keV at 511 keV). This broadening is characterized by two distinct parameters, S and W, defined as a fraction of the annihilation line in the middle (511 ± 0.70 keV) and outer regions (508.56 ± 0.30 keV and 513.44 ± 0.30 keV), respectively. The total area below the curve, which is utilized for normalization of both parameters, is 511 ± 16.24 keV. The S-parameter is a fraction of positrons annihilating with low momentum valence electrons and represents open and free volumes and their concentration. The W-parameter approximates the overlap of the positron wavefunction with high-momentum core electrons, hence provides a fingerprint of the chemical environment at the annihilation site. Plotting S and W as a function of positron implantation energy provides depth-dependent information, whereas S-W plots [30] are used to examine the atomic surroundings of the defect site and its size (type) [31].

Positrons implanted into solids may form a hydrogen-like bound state with an electron, the so-called positronium (Ps) [32, 33]. Ps is formed on external or internal surfaces of solids by a thermalized positron picking an electron on the surface and escaping from the solid into a pore or free space [34]. Depending on the orientation of electron and positron spin in the bound state, Ps decays in two photons (para-Ps, singlet-state) or three photons (ortho-Ps, triplet-state). In solids, the three-photon decay of ortho-Ps is suppressed due to pick-off annihilation (two-photon decay) with an electron with opposite spin from the environment [35, 36]. The lifetime of o-Ps will be reflected in the S-parameter and longer lifetime components (> 500 ps).

2.4 | XPS

All XPS analyses were carried out with a Thermo VG Scientific, type NEXSA G2, at nanoanalytics GmbH, Münster, Germany, in an ultra-high vacuum environment with a base pressure of $1 \times 10{-}9$ mbar. Core-level spectra were obtained using monochromatic Al-Kα radiation (1486.6 eV), 400 μm spot size.

The energy scale of the spectrometer was calibrated using copper, silver, and gold reference samples according to ISO15472:2001. The intensity scale was calibrated according to a procedure defined by the manufacturer of the instrument. This procedure was developed by the device manufacturer based on the literature by Hemminger [37] and Wicks [38]. Differential charging was minimized using the built-in flood gun (low-energy electrons and argon ions). Every sample was measured at two different spots.

Curve fitting of the Si 2p core level was performed following the methodology established by Alexander et al. [39], who demonstrated that meaningful quantitative analysis could be achieved even for XPS spectra lacking distinct spectral features. Four silicon binding states were defined based on the number of coordinated oxygen atoms, with binding energies determined using poly(dimethylsiloxane) (PDMS) and quartz (SiO_2) as reference standards. The following binding energies were assigned:

- $Si(\text{-}O)_1$ at 101.2 ± 0.1 eV
- $Si(\text{-}O)_2$ at 101.9 ± 0.1 eV (corresponding to the PDMS standard)
- $Si(\text{-}O)_3$ at 102.6 ± 0.1 eV
- $Si(\text{-}O)_4$ at 103.7 ± 0.1 eV (corresponding to the SiO_2 standard)

These four components represent silicon atoms in progressively more oxidized environments, ranging from silicon bonded to one oxygen atom (with three carbon/hydrogen substituents) to fully oxidized silicon in a silica-like tetrahedral coordination with four oxygen atoms. This approach enables quantitative determination of the silicon chemical environment distribution within plasma-deposited organosilicon films, providing insight into the degree of oxidation and cross-linking achieved during the deposition process.

2.5 | Oxygen Transmission Rate (OTR)

The OTRs tested at IKV in accordance with DIN 53380-3/ASTM 3985-02 by means of Model M8001, Systech Instruments Ltd. These tests are carried out at 23°C and 0% relative humidity. These measurements were performed on the samples R1−R5 to amend the already performed OTR measurements for V1−V8. Each test point was measured fourfold.

3 | Results

In the following, the key findings of XPS and positron annihilation spectroscopy (PAS) are presented and compared in an approach to aggregate the diverse dimensions of the coating's structural properties into a comprehensive overview. With this, the initial hypothesis is then tested.

3.1 | Chemical Composition

XPS measurements showed, as expected, that the elementary composition of all investigated coatings is dominated by Si, O, and C. The comprehensive list of all results is given in Table A1 in the appendix. The classification of coatings into "SiO_x" and "SiOCH" categories was based on their barrier performance characteristics established in previous investigations (Figure 1). This classification correlates directly with the silicon binding state distribution determined from XPS curve fitting analysis using the method of Alexander et al. described earlier [39]. As shown in Figure 2, SiO_x coatings are characterized by silicon peaks that are almost exclusively composed of highly oxidized $Si(-O)_4$ environments (orange), with binding energies approaching those of SiO_2, indicating nearly complete oxidation of the silicon atoms. In contrast, SiOCH coatings exhibit a more diverse silicon coordination environment, with significant contributions from lower oxidation states $Si(-O)_2$ (dark blue) and $Si(-O)_3$ (teal), reflecting the presence of silicon-carbon bonds and partially oxidized silicon species. This ranges from almost SiO_x-like coatings like V8 with a $Si(-O)_4$ share of $> 78\%$ to barely oxidized coatings like R3, where most silicon atoms have only one coordinated oxygen atom ($Si(-O)_1 > 63\%$) and fully oxidized silicon atoms are almost absent ($Si(-O)_4 < 2\%$). This distinct difference in silicon binding state distribution provides a reliable chemical basis for distinguishing between the two coating types, with the predominance of $Si(-O)_4$ serving as a clear indicator of SiO_x character, while mixed oxidation states with substantial $Si(-O)_2$ and $Si(-O)_3$ contributions are characteristic of SiOCH coatings.

In order to summarize the XPS measurements, Figure 3 compares the elementary composition of all coatings without considering the chemical shifts. It is evident that the data for all elements strongly correlate linearly (R^2 is 0.99 for C/O, 0.88 for Si/O, and 0.93 for Si/C), which suggests that the PECVD coating process yields chemical compositions only within a defined framework. Thus, describing any of the coatings considered with the at% of only one element is sufficient to estimate the other contents within a reasonable margin of error (i.e., a coating within the considered framework with 30 at% Si will most likely consist of 50 at% O and 20 at% C). This steady shift in stoichiometry implies that a differentiation between SiO_x and SiOCH is not possible on this basis without additional information. It turned out that the silicon share is most helpful in explaining the following investigations; it is thus used as a marker for coating chemistry.

3.2 | Porous Structure

Spectra from VEPALS are decomposed into three pore categories that are characterized each by a lifetime τ_i (as long as $\tau_i > 500\,ps$) and the corresponding signal intensity I_i. It is reasonable to assume it as proportional to the porosity (i.e., the volume share of pores) of the coating in the corresponding pore size range [40, 41]. Figure 4 shows the depth-resolved data on τ_2 for all investigated samples. Since the coatings have different thicknesses and densities, the implementation depth is expressed as implementation energy E_p to reduce data distortion. Thus, it should be kept in mind that data points for different coatings acquired with the same implementation energy do not necessarily stem from the same distance to the surface. However, even when taking into account the measurement uncertainties, it seems reasonable to assume that an interface zone (as described in earlier works [40]) is present for $4\,keV \leq E_p \leq 6\,keV$, while data with $E_p > 6\,keV$ results from the pure gold substrate. This is supported by lifetime and intensity data of all pore categories, which are not shown here.

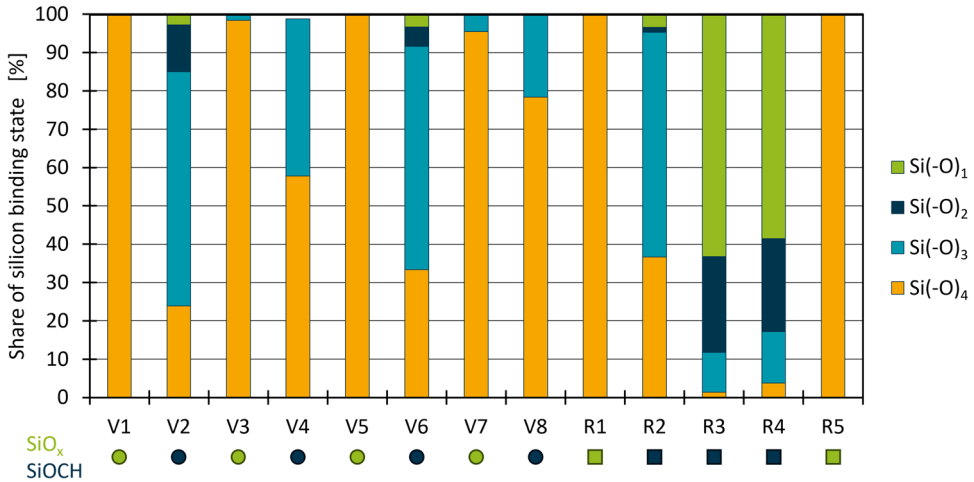

FIGURE 2 | Chemical shift of Si for all samples, categorized in four binding states based on the number of coordinated oxygen atoms. On the bottom, each sample is assigned to either SiO_x (green) or SiOCH (blue).

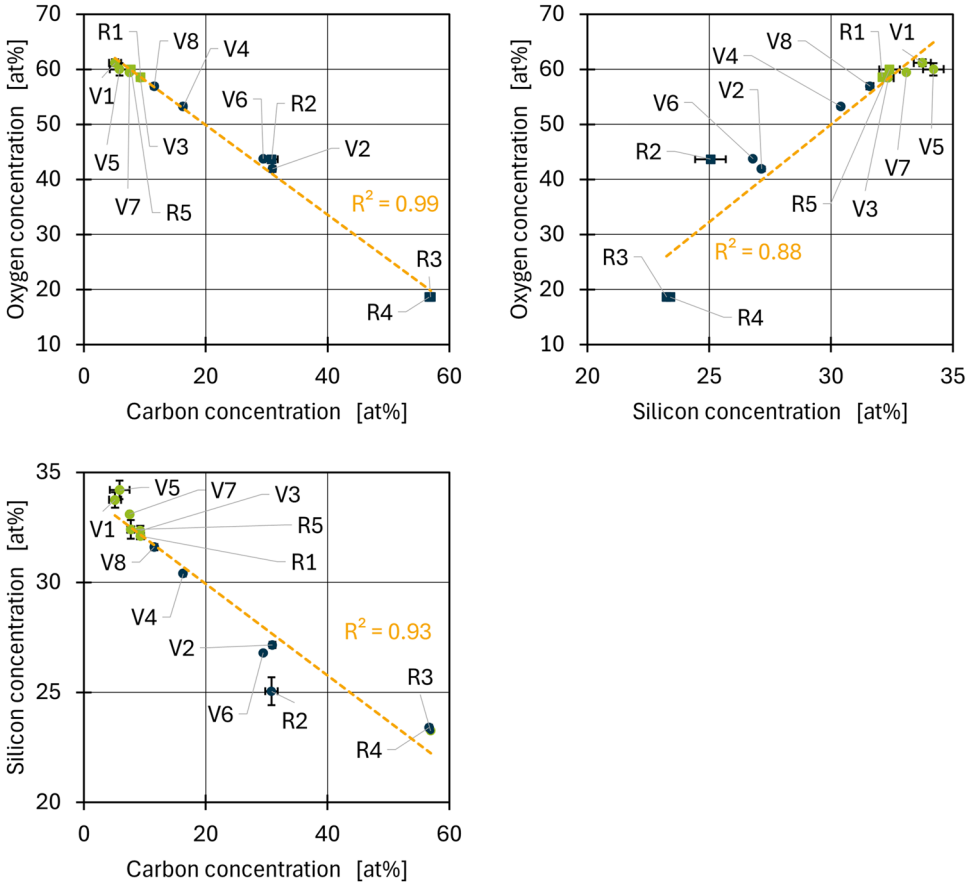

FIGURE 3 | Comparison of Si, O, and C contents of all coatings.

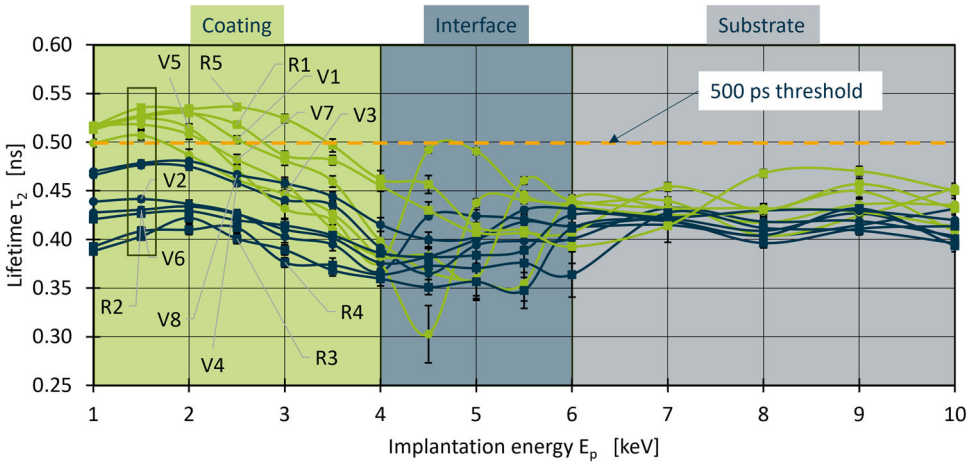

FIGURE 4 | Depth-resolved data on lifetime component τ_2 for all SiO_x (green) and SiOCH coatings (blue).

For further analysis, only data from $E_p = 1.5keV$ (marked by the green box in Figure 4) is considered in the following, as the observed effects are best seen here, and it is sufficiently distant from both the surface and the interface zone to mitigate interference effects. In Figure 4, a distinction between SiO_x and SiOCH can already be observed. At $E_p = 1.5keV$, only for the SiO_x coatings, $\tau_2 > 500ps$ is the case. In terms of PAS, this means that only SiO_x seems to have pores in this pore category (pore diameter d_P of ~0.28 nm). This threshold stems from the size of ortho-Ps, which requires a minimum space of that size. The case is only fulfilled for lifetimes $> 500ps$. Below that threshold, a differentiation between pores and other voids, such as vacancy clusters, becomes increasingly fuzzy. All identified lifetime components that resulted from PALS spectra deconvolution are listed in Table 2. For each category, the range of lifetime τ_i and intensity I_i for an implantation energy of $E_p = 1.5\ keV$ is summarized, and their significance is stated. All data points on lifetime and intensity for all categories (@1.5 keV) can be found in the Appendix, Table A2.

τ_1 results mostly from para-Positronium, which has a short intrinsic lifetime because its positron will annihilate with its

TABLE 2 | PALS spectra deconvolution categories. Only categories 2–4 were identified as pore-related.

i	Lifetime τ_i range [ns]	Intensity I_i range [%]	Significance
1	0.13–0.20	10–15	p-Ps contribution (sub-pore regime)
2	0.40–0.54	54–70	Vacancy agglomerations & smallest detected micropores
3	1.4–1.8	12–26	Micropores
4	2.3–4.5	4–11	Micropores
5	15–23	0.4–2.8	o-Ps contribution from the surface

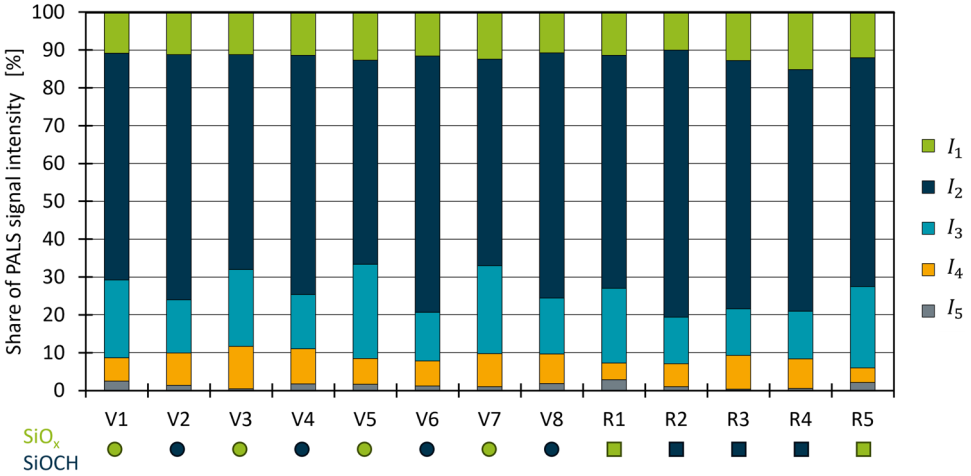

FIGURE 5 | Overview of all signal intensities @ 1.5 keV. On the bottom, each sample is assigned to either SiO_x (green) or SiOCH (blue).

own bound electron in ~125 ps in vacuum. Since it does not interact with the sample, its correlation with pore parameters is limited, and thus, τ_1 will not be further considered in the scope of this work. τ_2 is a result of both vacancy agglomerations (SiOCH) and the smallest detected micropores (SiO_x). Its signal intensity is the highest from all lifetime components, which underscores its importance to understand the porous structure of our samples. τ_3 and τ_4 stem from larger micropores ($d_{P3} \sim 0.52\ nm$ and $d_{P4} \sim 0.76\ nm$). τ_5 represents a surface state, as it results from o-Ps escaping the sample into the vacuum, and thus does not provide useful information on the porous structure. Like τ_1, it will not be considered in the following.

In Figure 5, an overview is given for all intensities of all samples. It is evident that the relevant categories 2–4 make up the majority of signals, which is dominated by category 2. Consistent with Figure 2, all samples are labeled as either SiO_x or SiOCH. Intensities I_2 and I_3 prove as good discriminators for SiO_x ($I_2 < 62\%$ and $I_3 > 19\%$) and SiOCH ($I_2 > 63\%$ and $I_3 < 15\%$), which indicates significant differences in their porous structure.

The results from DB-VEPAS are summarized in Figure 6. Both S- and W-parameter exhibit characteristic anticorrelated shapes (high S value corresponds to low W and vice versa) that indicate a depth-dependent change in structure that is more pronounced than what VEPALS data suggest (see Figure 4). S reaches a maximum value in a range of $E_p = 1.5...2\ keV$ before converging towards its minimum at $E_p \sim 4\ keV$, W accordingly develops inverted. For both, SiO_x and SiOCH are well distinguishable near the surface and converge towards the substrate. For the S-parameter, this is shown by the significantly lower maximum for the SiO_x coatings, indicating a lower porosity, although this

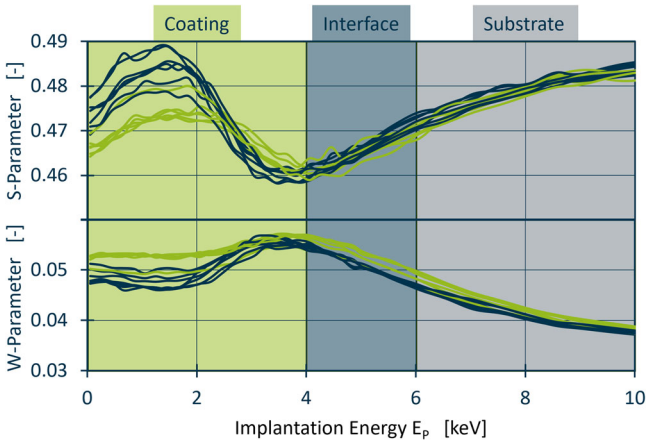

FIGURE 6 | S- and W-parameter data from DB-VEPAS measurements of SiO_x (green) and SiOCH (blue) coatings.

can only be stated qualitatively. For the W-parameter, on the other hand, the SiO_x curves have a significantly different shape, where they almost remain constant, while the SiOCH curves show a clear minimum. For both S and W, all curves overlap at $E_p \sim 4keV$ and start to converge, similar to Figure 4, towards the substrate properties. The S-parameter for SiO_x films does not follow the changes of average positron lifetime, whereas SiOCH seems to have a higher porosity based purely on larger S. The low value of S for SiO_x is puzzling but is likely a consequence of the somehow different sensitivity of the DB-VEPAS method to o-Ps annihilation compared to VEPALS for systems with high positron-to-Ps conversion. In general, the S-parameter has a higher sensitivity to defect concentration and less to pores. In

the case of SiO_x films, an extreme case is encountered, where most of the defected PALS signals from the top half of the film originate from pore structures. As for the VEPALS data, only data from $E_p = 1.5\,keV$ is considered in the following discussion.

4 | Discussion

In order to obtain a quantitative measure of porosity, a porosity index φ is derived from signal categories 3 and 4, then normalized to a maximum value (which was found for sample V5, so $\varphi_{norm}(V5) = 1$):

$$\varphi = I_3 \bullet \tau_3 + I_4 \bullet \tau_4 \varphi_{norm} = \frac{\varphi}{\varphi_{\max}} \quad (4)$$

The normalized porosity index φ_{norm} provides a relative measure of porosity compared to the most porous sample (V5), considering contributions from both micropores of signal categories 3 and 4. Signal category 2 is excluded because it encompasses both vacancy agglomerations in SiOCH and small micropores in SiO_x, making it unsuitable for distinguishing material-specific porosity characteristics. It is possible that the reduced τ_2 observed for SiOCH results from o-Ps quenching—a process where the o-Ps state is eliminated through interactions (e.g., magnetic fields or chemical reactions) with the local environment, leading to significant lifetime reduction. This mechanism differs from pick-off annihilation, where the o-Ps state remains intact until the positron annihilates with an external electron. However, the extent to which o-Ps quenching influences τ_2 in SiOCH remains unclear, as this would require residual reactivity such as radicals or paramagnetic defect centers capable of facilitating spin exchange or chemical reactions with positronium atoms.

Since category 2 exhibits the highest intensity and therefore dominates the overall signal, lifetime τ_2 is examined alongside the porosity index φ_{norm}. Both parameters are compared with the silicon concentration from XPS in Figure 7.

It reveals several critical insights into the relationship between chemical composition and material structure. The data exhibits a distinct threshold behavior at approximately 32 at% silicon concentration, above which the material transitions from SiOCH to SiO_x character. This compositional threshold coincides with a corresponding threshold in the positron lifetime τ_2 at ~500 ps, suggesting a fundamental change in the local electronic environment and defect structure at this critical composition.

The strong correlation between silicon concentration and τ_2 ($R^2 = 0.93$) demonstrates that positron annihilation is highly sensitive to the chemical composition and local bonding environment. The threshold at ~500 ps likely reflects the transition from a carbon-rich SiOCH matrix with specific vacancy-type defects to a more silica-like SiO_x structure. This threshold behavior may also be related to the o-Ps quenching effects discussed previously, where the change in chemical environment at higher silicon concentrations introduces different types of paramagnetic centers or reactive sites that alter positron annihilation dynamics. Contrary to expectations, the normalized porosity index tends to be higher for SiO_x materials, despite the absence of a clear threshold as observed for τ_2. This finding is particularly intriguing because SiO_x materials typically exhibit barrier properties that should correlate with lower porosity. The weaker correlation between silicon concentration and porosity ($R^2 = 0.65$) compared to the τ_2 relationship suggests that the porosity is influenced by additional factors beyond simple compositional changes.

These results indicate that while pores undoubtedly contribute to coating permeability, their influence appears negligible compared to the chemical structure of the bulk matrix. The strong correlation with silicon concentration and the threshold effects suggest that the atomic-scale bonding environment and defect chemistry play dominant roles in determining material performance. This insight has important implications for material design, suggesting that optimizing barrier properties requires careful control of chemical composition and local bonding structure rather than simply minimizing porosity. It should be noted that other datapoints from XPS and PAS measurements could have been shown for similar insights, but the presentation would have been less clear. Nevertheless, most datapoints suggest a smooth transition from SiOCH to SiO_x (e.g., it seems as if increasing the silicon share would lead to a continuous shift). Since the definition of both coating types is somewhat vague and they basically are both chemical structures with a silicon-oxidic backbone and varying organic

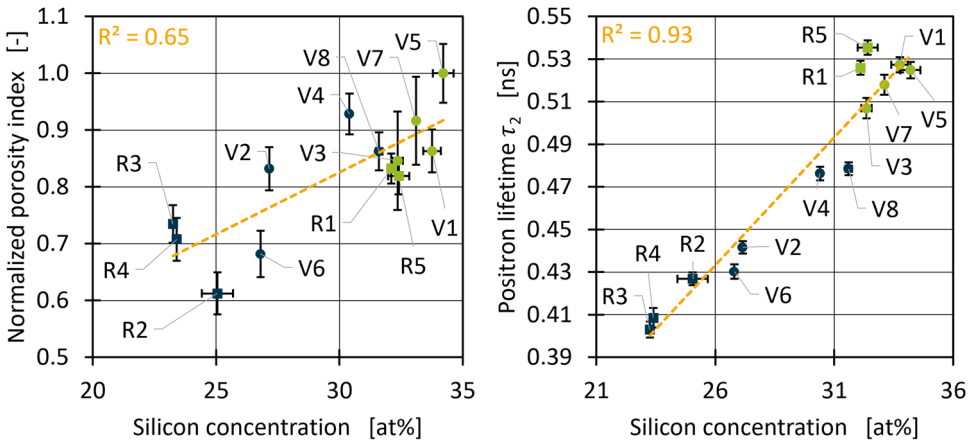

FIGURE 7 | Silicon share of all coatings compared with the summed-up intensities of pore-related signal categories 3–5 and positron lifetime τ_2 (SiO_x in green, SiOCH in blue).

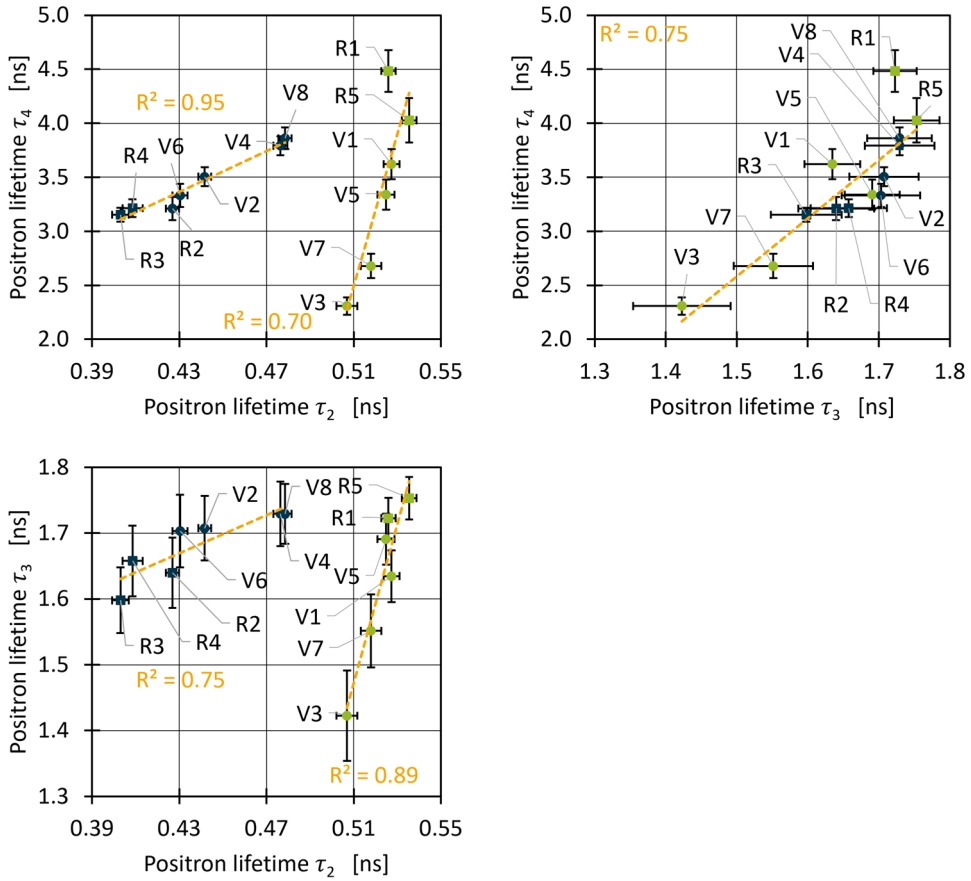

FIGURE 8 | Comparison of positron lifetimes 2, 3, and 4 for all coatings (SiO_x in green, SiOCH in blue).

content, this is not unexpected. However, this does not explain the sudden emergence of the barrier property of SiO_x.

This issue can be addressed by a more detailed investigation of the different pore sizes, which reveals significant differences between SiO_x and SiOCH. Figure 8 compares positron lifetimes (more specifically positron and o-Ps lifetimes) of the categories 2, 3, and 4, which are correlated with the respective pore/defect sizes. When comparing τ_3 and τ_4, which represent the most prevalent pore categories, both SiO_x and SiOCH show a positive correlation. A good metaphor for this is a household sponge, in which both small and large pores expand equally when stretched. This is not observed when comparing either τ_3 or τ_4 to the lifetime τ_2: In both cases, an increase in one of them also leads to an increase of τ_2 for SiOCH, but for SiO_x, τ_2 barely changes—even more so, the continuous shift seen before in many different properties is no longer present. Considering the chemical composition, an increasing silicon share (see Figure 7) seems to continuously shift the structure of a SiOCH coating towards SiO_x properties (best seen for samples V4 and V8)—once SiO_x properties are obtained (in a discontinuous manner!), the structure (represented by τ_2) seems largely fixed, while the size of larger micropores (τ_3 and τ_4) can still vary.

The results demonstrate that SiO_x and SiOCH coatings resemble each other in most properties, and their porosity and pore size exert at most a secondary influence on their gas barrier performance. Nonetheless, especially τ_2 seems to contain valuable information on the chemical structure, as it correlates very strongly with the silicon share and shows a discontinuous shift from SiOCH to SiO_x when compared to other positron lifetime components. This is supported by the findings of Inoue et al. [42], who investigated different silica-based glasses and pure SiO_2. In their studies, they found mean values of $\tau_2 = 0.7$ ns and $I_2 = 14$ % for SiO_2. The higher the molar fraction of SiO_2 in the other glasses, the more their values for τ_2 and I_2 would approach those of SiO_2. This tendency is also observed for SiO_x and SiOCH, where SiO_x is structurally closer to SiO_2. This is also reflected in the XPS measurements showing Si-binding states almost exclusively resembling SiO_2 for the SiO_x samples (see Figure 2).

Figure 9 depicts the relation of S and W parameters with the silicon share of the coatings. Parts of these results have been shown earlier [19] and are now extended. While S and W are strongly correlated linearly ($R^2 = 0.85$), indicating a similar defect type for all samples [43], this similarity becomes even more pronounced upon detailed examination of the plot. First, it is evident that most SiO_x coatings (except R1) are clustered in a small area of high W and low S, while the SiOCH coatings are more spread out, a pattern which can also be seen in Figure 7. Moreover, differentiating between R and V samples instead, R^2 increases to 0.89 and 0.99, respectively. This indicates that while all coatings seem to have a similar defect type, two groups can be spotted, which result from slightly different PECVD process parameters. Furthermore, W, a measure of pore wall chemistry, is strongly correlated with the silicon share. This implies that the silicon share exerts more influence on the pore wall chemistry than oxygen or carbon shares, even if it is not the single defining parameter for it.

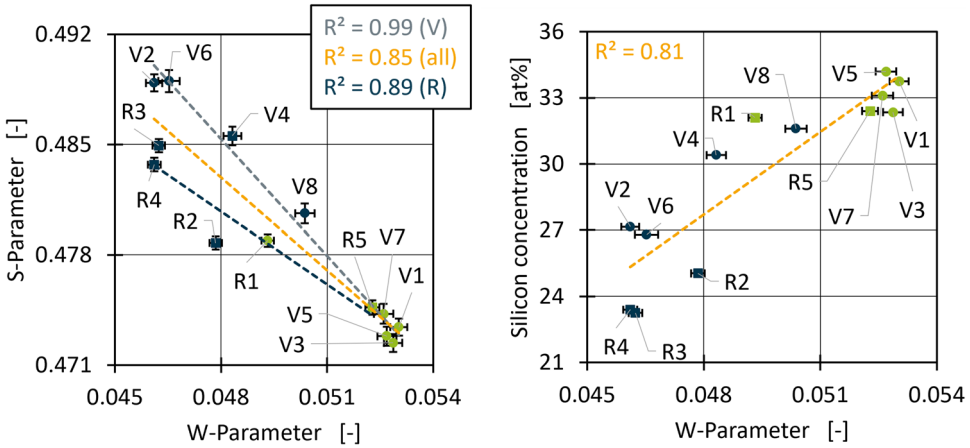

FIGURE 9 | Comparison of S and W parameters from DB-VEPAS with the silicon share (SiO_x in green, SiOCH in blue).

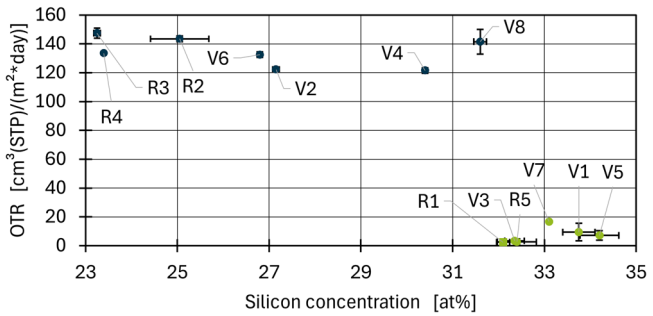

FIGURE 10 | OTR compared to the silicon share.

The initial hypothesis proposed that the C/O ratio would be a critical parameter for the coating's properties. Nevertheless, the data analysis revealed that the silicon share is better suited for all comparisons. While the C/O ratio can be used to yield similar conclusions (not shown here), the silicon concentration provides clearer correlations. In that sense, characterizing the C/O ratio as "a critical, but not the best parameter" would be more precise. The analysis demonstrated that chemical composition significantly influences porous structure.

The second statement of the hypothesis was on the binary nature of the relationship between chemical composition and barrier performance, which is well recognizable in Figure 10 (the uncoated PET has an OTR of 154 $\pm$ $4\frac{cm^3(STP)}{m^2 day}$). Below 32 at% Si, all coatings are attributed to the SiOCH group and thus show no barrier property, whereas all SiO_x coatings are > 32 at% Si (The same is true for C/O, where the threshold is at ~0.2). Note that the Si threshold is quite sharp OTR-wise, with V8 at 31.6 at% and R1 at 32.1 at%. This difference of 0.5 at% approaches the typical uncertainty of XPS quantification.

Remarkably, most of the data analyzed in this work revealed steady/continuous relationships of different coating properties with their silicon share, with the only exceptions of the positron lifetimes τ_3 and τ_4. While τ_2 is strongly correlated with Si, these lifetime values clearly evolve in a discontinuous way (see Figure 8). At this point, focusing on the samples V4 and V8, both SiOCH, can help us understand. Except for positron lifetimes, all SiO_x samples tend to cluster in a small range, while SiOCH coatings are more varied. The fact that they have been produced with large variations in energy densities (e.g., compare V4 and R4 in Figure 1) can at most explain some variations in properties: V2, V4, V6, and V8 have very similar energy densities and yet show large variations in XPS, VEPALS, and DB-VEPAS data. In many plots, V4 and V8 are very close to the SiO_x cluster. In Figure 2, V4 and V8 show the by far highest shares of $Si(-O)_4$ binding state of all SiOCH coatings, which is very strongly correlated logarithmically with their carbon share (see Figure 11).

As carbon content increases, there's a logarithmic decrease in fully oxidized silicon sites. This suggests that carbon and oxygen are competing for bonding sites on silicon atoms. The logarithmic curve suggests that at low carbon concentrations, small increases dramatically reduce $Si(-O)_4$ formation, but at higher carbon levels, the effect becomes less pronounced. This indicates the system approaches a saturation point where further carbon incorporation has diminishing impact on silicon oxidation. By continuously decreasing the carbon share (or increasing the silicon share, see Figure 3) of a SiOCH coating, the properties of a SiO_x are approached, but reached only after what appears to be a structural reorganization of the coating's molecular architecture. This reorganization could result from the absence of any Si-C bonds in SiO_x, which have much lower bond energy (318 vs. 452 kJ/mol) and longer bond length (185 vs. 163 pm) [44]. This will most likely result in a more rigid, homogeneous structure as the Si-O bonds tend to organize in a cage structure with a Si-O-Si angle of 150° [45]. This was also observed by Kleines et al. [46], who noticed a shift from network (bond angle 144°) to cage structures of the Si-O-Si bonds with increasing oxygen flow during the PECVD process. The smaller bond angle in SiOCH network structures might lead to the smaller positron lifetime values from VEPALS, but without further research, this remains speculative.

Using the Tao-Eldrup model [35, 36], the pore size d_2 calculated from τ_2 is in the diameter range of 0.27 nm $\leq d_2 \leq$ 0.29 nm for the SiO_x, which is close to the theoretical size of a cubic cage structure with a bond angle of 150° and a Si-O mean bond length of 1.64 Å [47], for which a cube size is calculated to 317 pm. The suggestion that τ_2 results from a dominant cage structure in SiO_x could be drawn from this, but it does not take the residual carbon share into account. Since the Si atoms in SiO_x have almost exclusively the highest oxidation state $Si(-O)_4$, the assumption is made that for them, almost no Si-C bonds are present, but Si-O bonds are prevalent. This implies that the

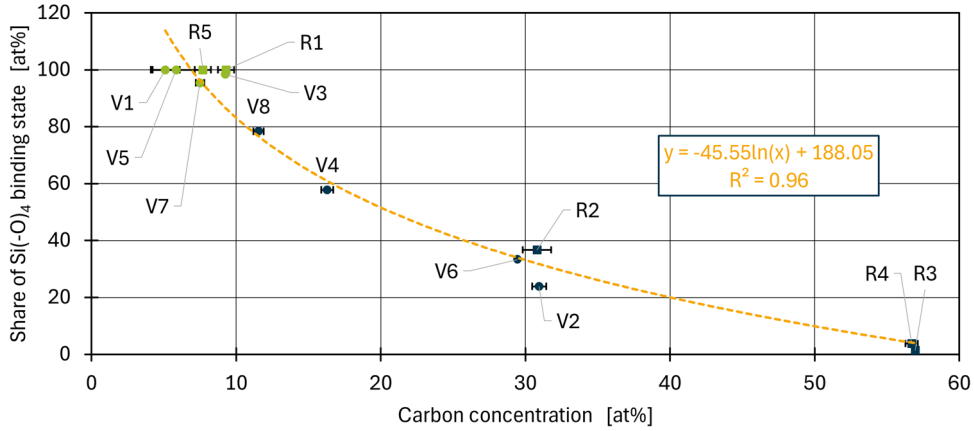

FIGURE 11 | Si3 share compared to the carbon share for SiOCH coatings.

remaining carbon in SiO_x is mostly bonded directly to oxygen, in the form of Si-O-C. The homogeneity of the cage structure would be disturbed at these points, possibly leading to the creation of larger defects.

5 | Conclusion

In this work, 13 coating systems were analyzed extensively using VEPALS, DB-VEPAS, and XPS, complemented by earlier investigations on the same coatings. The analysis reveals two distinct coating groups: SiOCH coatings with silicon-oxidic structures containing substantial organic content, and SiO_x coatings with only residual organic content. These groups are clearly distinguishable across multiple properties, including oxygen permeability, positron lifetimes (corresponding to pore sizes), porosities, and chemical composition.

The data largely support the proposed threshold hypothesis. While most coating properties show gradual transitions between the two groups, some properties demonstrate clear threshold behavior: oxygen permeability (Figure 10), positron lifetime relationships (τ_2 vs. τ_3 and τ_2 vs. τ_4, Figure 8), and silicon binding states (Figure 2) all exhibit distinct transitions rather than continuous changes.

Although the silicon content proved more effective than the C/O ratio for data presentation, this does not invalidate the underlying threshold principle. The silicon parameter and C/O ratio are fundamentally related measures of coating organicity, and both reveal the same threshold behavior in barrier performance.

The key structural difference between SiOCH and SiO_x lies in carbon incorporation. In SiOCH coatings, abundant carbon forms direct Si-C bonds, while in SiO_x coatings, minimal carbon content connects to silicon indirectly through Si-O-C linkages. This difference in carbon bonding fundamentally alters the bulk matrix structure and its relationship to porosity. Importantly, the decisive factor for barrier performance is not pore size alone, but the coating's chemical structure and mode of carbon incorporation, which changes abruptly at the threshold rather than gradually.

Acknowledgements

The work shown in this paper was funded by the Deutsche Forschungsgemeinschaft (DFG, German Research Foundation)—Project No. 542661390. We would like to thank the DFG. Parts of this research were carried out at ELBE at the Helmholtz-Zentrum Dresden–Rossendorf. V., a member of the Helmholtz Association. We would like to thank the facility staff for their assistance. This work was partially supported by the Initiative and Networking Fund of the Helmholtz Association (FKZ VH-VI-442 Memriox) and the Helmholtz Energy Materials Characterization Platform (03ET7015).

Conflicts of Interest

The authors declare no conflicts of interest.

Data Availability Statement

The data that support the findings of this study are available from the corresponding author upon request.

References

1. T. d l Arcos, P. Awakowicz, M. Böke, et al., "PECVD and PEALD on Polymer Substrates (Part II): Understanding and Tuning of Barrier and Membrane Properties of Thin Films," *Plasma Processes & Polymers* 21, no. 3 (2024): 2300186, https://doi.org/10.1002/ppap.202300186.

2. R. Snyders, D. Hegemann, D. Thiry, O. Zabeida, J. Klemberg-Sapieha, and L. Martinu, "Foundations of Plasma Enhanced Chemical Vapor Deposition of Functional Coatings," *Plasma Sources Science and Technology* 32, no. 7 (2023): 074001.

3. S.-K. Cho, T.-Y. Cho, W. J. Lee, et al., "Gas Barrier and Mechanical Properties of a Single-Layer Silicon Oxide Film Prepared by Roll-to-Roll PECVD System," *Plasma Processes & Polymers* 16, no. 4 (2019): 1800170, https://doi.org/10.1002/ppap.201800170.

4. Global Market Insights. Barrier Coatings for Packaging Market—By Type, by Technology, by Functionality, by End Use & Forecast, 2024−2032, GMI11767, 2024.

5. Coherent Market Insights. Chemical Vapor Depostion Market Size and Share Analysis—Growth Thrends and Forecasts (2025−2023), CMI7424, 2025.

6. A. Bieder, A. Gruniger, and R. von Rohr, "Deposition of SiOx Diffusion Barriers on Flexible Packaging Materials by PECVD," *Surface and Coatings Technology* 200, no. 1–4 (2005): 928–931.

7. D. Framil, M. van Gompel, F. Bourgeois, I. Furno, and Y. Leterrier, "The Influence of Microstructure on Nanomechanical and Diffusion Barrier Properties of Thin PECVD SiOx Films Deposited on Parylene C Substrates," *Frontiers in Materials* 6 (2019): 319, https://doi.org/10.3389/fmats.2019.00319.

8. E. Vassallo, M. Pedroni, M. Aloisio, et al., "Plasma Deposition to Improve Barrier Performance of Biodegradable and Recyclable Substrates Intended for Food Packaging," *Plasma* 5, no. 4 (2022): 451–461.

9. D. Hegemann, "Plasma Polymer Deposition and Coatings on Polymers." *Comprehensive Materials Processing* (Elsevier, 2014), 201–228.

10. A. Grüniger, A. Bieder, A. Sonnenfeld, P. R. von Rohr, U. Müller, and R. Hauert, "Influence of Film Structure and Composition on Diffusion Barrier Performance of SiOx Thin Films Deposited by PECVD," *Surface and Coatings Technology* 200, no. 14–15 (2006): 4564–4571.

11. R. Morent, N. De Geyter, S. Van Vlierberghe, et al., "Deposition of HMDSO-Based Coatings on PET Substrates Using an Atmospheric Pressure Dielectric Barrier Discharge," *Progress in Organic Coatings* 64, no. 2–3 (2009): 304–310.

12. D. Hegemann, H. Brunner, and C. Oehr, "Improving the Adhesion of Siloxane-Based Plasma Coatings on Polymers With Defined Wetting Properties," in *45th Annual Technical Conference Proceedings (2002)*. Society of Vacuum Coaters, (2002).

13. J. Shim, H. G. Yoon, S.-H. Na, I. Kim, and S. Kwak, "Silicon Oxynitride Gas Barrier Coatings on Poly(Ether Sulfone) by Plasma-Enhanced Chemical Vapor Deposition," *Surface and Coatings Technology* 202, no. 13 (2008): 2844–2849.

14. K.-W. Lu, H.-L. Chen, H.-P. Chen, and C.-C. Kuo, "Design of Organic/Inorganic Multilayer Water Vapor Barrier Thin Films Deposited via Plasma Polymerization for Encapsulation," *Thin Solid Films* 767 (2023): 139672.

15. A. Patelli, S. Vezzù, L. Zottarel, et al., "SiOx-Based Multilayer Barrier Coatings Produced by a Single PECVD Process," *Plasma Processes & Polymers* 6 (2009): S1.

16. C.-Y. Wu, R.-M. Liao, L.-W. Lai, M.-S. Jeng, and D.-S. Liu, "Organosilicon/Silicon Oxide Gas Barrier Structure Encapsulated Flexible Plastic Substrate by Using Plasma-Enhanced Chemical Vapor Deposition," *Surface and Coatings Technology* 206, no. 22 (2012): 4685–4691.

17. L. E. Nielsen, "Models for the Permeability of Filled Polymer Systems," *Journal of Macromolecular Science: Part A—Chemistry* 1, no. 5 (1967): 929–942.

18. P. Alizadeh, J. Franke, and R. Dahlmann, "Stretch-Tolerant PECVD Gas Barrier Coatings for Sustainable Flexible Packaging," *Plasma Processes & Polymers* 21, no. 8 (2024): e2400018, https://doi.org/10.1002/ppap.202400018.

19. J. Franke, M. O. Liedke, P. Dahmen, et al., "Influence of Coating Structure of an Siox Barrier Coating on a PET Substrate on Water Vapor Permeation Activation Energy," *Ediciones Uniandes* 39 (2024), https://doi.org/10.51573/Andes.PPS39.GS.NN.1.

20. S. Kiese, E. Kücükpinar, O. Miesbauer, and H.-C. Langowski, "The Influence of Temperature on the Intrinsic Transport Properties of Water in Inorganic and Polymeric Coatings," *Thin Solid Films* 717 (2021): 138476.

21. A. P. Roberts, B. M. Henry, A. P. Sutton, et al., "Gas Permeation in Silicon-Oxide/Polymer (SiOx/PET) Barrier Films: Role of the Oxide Lattice, Nano-Defects and Macro-Defects," *Journal of Membrane Science* 208, no. 1–2 (2002): 75–88.

22. D. Kirchheim, S. Wilski, M. Jaritz, et al., "Improved Homogeneity of Plasma and Coating Properties Using a Lance Matrix Gas Distribution in MW-PECVD," *Journal of Coatings Technology and Research* 16, no. 2 (2019): 573–583.

23. A. Wagner, M. Butterling, M. O. Liedke, K. Potzger, and R. Krause-Rehberg, "Positron Annihilation Lifetime and Doppler Broadening Spectroscopy at the ELBE Facility." *International Workshop on Physics With Positrons at Jefferson Lab* (AIP Publishing, 2018), 40003.

24. E. Hirschmann, M. Butterling, U. Hernandez Acosta, et al., "A New System for Real-Time Data Acquisition and Pulse Parameterization for Digital Positron Annihilation Lifetime Spectrometers With High Repetition Rates," *Journal of Instrumentation* 16, no. 08 (2021): P08001.

25. R. Krause-Rehberg and H. S. Leipner, *Positron Annihilation in Semiconductors: Defect Studies; With 20 Tables*. Springer, (2003), 379.

26. J. V. Olsen, P. Kirkegaard, N. J. Pedersen, and M. Eldrup, "PALSfit: A New Program for the Evaluation of Positron Lifetime Spectra," *Physica Status Solidi C* 4, no. 10 (2007): 4004–4006.

27. M. O. Liedke, W. Anwand, R. Bali, et al., "Open Volume Defects and Magnetic Phase Transition in Fe60Al40 Transition Metal Aluminide," *Journal of Applied Physics* 117, no. 16 (2015): 163908, https://doi.org/10.1063/1.4919014.

28. W. Anwand, G. Brauer, M. Butterling, H. R. Kissener, and A. Wagner, "Design and Construction of a Slow Positron Beam for Solid and Surface Investigations," *Defect and Diffusion Forum* 331 (2012): 25–40.

29. J. Dryzek and P. Horodek, "GEANT4 Simulation of Slow Positron Beam Implantation Profiles," *Nuclear Instruments and Methods in Physics Research Section B: Beam Interactions With Materials and Atoms* 266, no. 18 (2008): 4000–4009.

30. I. Makkonen and F. Tuomisto, "Perspective on Defect Characterization in Semiconductors by Positron Annihilation Spectroscopy," *Journal of Applied Physics* 135, no. 4 (2024): 040901, https://doi.org/10.1063/5.0180024.

31. M. Clement, J. M. M. de Nijs, P. Balk, H. Schut, and A. van Veen, "Analysis of Positron Beam Data by the Combined Use of the Shape- and Wing-Parameters," *Journal of Applied Physics* 79, no. 12 (1996): 9029–9036.

32. M. Charlton and J. W. Humberston, *Positron Physics*," (Cambridge University Press, 2001), 454.

33. O. E. Mogensen, *Positronium Formation in Condensed Matter and High-Density Gases* (North-Holland, 1982).

34. C. H. Hodges and M. J. Stott, "Work Functions for Positrons in Metals," *Physical Review B* 7, no. 1 (1973): 73–79.

35. M. Eldrup, D. Lightbody, and J. N. Sherwood, "The Temperature Dependence of Positron Lifetimes in Solid Pivalic Acid," *Chemical Physics* 63, no. 1–2 (1981): 51–58.

36. S. J. Tao, "Positronium Annihilation in Molecular Substances," *Journal of Chemical Physics* 56, no. 11 (1972): 5499–5510.

37. C. S. Hemminger, T. A. Land, A. Christie, and J. C. Hemminger, "An Empirical Electron Spectrometer Transmission Function for Applications in Quantitative XPS," *Surface & Interface Analysis* 15, no. 5 (1990): 323–327.

38. R. C. Wicks and N. J. C. Ingle, "Characterizing the Detection System Nonlinearity, Internal Inelastic Background, and Transmission Function of An Electron Spectrometer for Use in X-Ray Photoelectron Spectroscopy," *Review of Scientific Instruments* 80, no. 5 (2009): 53108.

39. M. R. Alexander, R. D. Short, F. R. Jones, W. Michaeli, and C. J. Blomfield, "A Study of HMDSO/O2 Plasma Deposits Using a High-Sensitivity and -Energy Resolution XPS Instrument: Curve Fitting of the Si 2p Core Level," *Applied Surface Science* 137, no. 1–4 (1999): 179–183.

40. J. Franke, F. Zysk, S. Wilski, et al., "Consideration of the Effect of Nanoscale Porosity on Mass Transport Phenomena in PECVD Coatings," *Journal of Physics D: Applied Physics* 57, no. 40 (2024): 405303.

41. D. W. Gidley, H.-G. Peng, and R. S. Vallery, "Positron Annihilation as a Method to Characterize Porous Materials," *Annual Review of Materials Research* 36, no. 1 (2006): 49–79.

42. K. Inoue, H. Kataoka, Y. Nagai, M. Hasegawa, and Y. Kobayashi, "Short and Medium Range Order in Two-Component Silica Glasses by Positron Annihilation Spectroscopy," *Journal of Applied Physics* 115, no. 20 (2014): 204903, https://doi.org/10.1063/1.4878457.

43. L. T. Son, T.-T. Doan, P. T. Phuc, et al., "Positron Annihilation Study of Lattice Defects and Nanoporous Structures in Mn4+ Doped K2SiF6 Nanophosphors Exhibiting High Quantum Yield," *Radiation Physics and Chemistry* 195 (2022): 110064.

44. J. J. Petkowski, W. Bains, and S. Seager, "On the Potential of Silicon as a Building Block for Life," *Life* 10, no. 6 (2020): 84.

45. A. Grill and D. A. Neumayer, "Structure of Low Dielectric Constant to Extreme Low Dielectric Constant Sicoh Films: Fourier Transform Infrared Spectroscopy Characterization," *Journal of Applied Physics* 94, no. 10 (2003): 6697–6707.

46. L. Kleines, S. Wilski, P. Alizadeh, et al., "Structure and Gas Separation Properties of Ultra-Smooth PE-CVD Silicon Organic Coated Composite Membranes," *Surface and Coatings Technology* 421 (2021): 127338.

47. W. H. Baur, "The Prediction of Bond Length Variations in Silicon-Oxygen Bonds," *American Mineralogist* 56, no. 9–10 (1971): 1573–1599.

Appendix

See Tables A1 and A2.

TABLE A1 | Elemental composition and Si2p deconvolution results of the sample surface (in at%/%) as determined by XPS measurements.

	O	C	Si	N	$Si(-O)_1$	$Si(-O)_2$	$Si(-O)_3$	$Si(-O)_4$
V1	61.2	5.1	33.7	0	0	0	0	100.0
V2	41.9	31.0	27.2	0	2.8	12.2	61.1	23.9
V3	58.4	9.3	32.4	0	0	0	1.6	98.4
V4	53.2	16.3	30.4	0	0	0	41.0	57.8
V5	60.0	5.8	34.2	0	0	0	0	100.0
V6	43.8	29.4	26.8	0	3.3	5.0	58.3	33.4
V7	59.4	7.5	33.1	0	0	0	4.4	95.4
V8	56.9	11.5	31.6	0	0	0	21.5	78.4
R1	58.6	9.3	32.1	0	0	0	0	100.0
R2	43.6	30.8	25.1	0.6	3.4	1.3	58.6	36.7
R3	18.6	56.9	23.2	1.2	63.2	25.0	10.3	1.4
R4	18.7	56.7	23.4	1.3	58.7	24.2	13.3	3.8
R5	59.9	7.7	32.4	0	0	0	0	100.0

TABLE A2 | Positron lifetime and signal intensities from VEPALS for components 1-5 for all samples at an implantation energy of 1.5 keV.

	τ_1 [ns]	I_1 [%]	τ_2 [ns]	I_2 [%]	τ_3 [ns]	I_3 [%]	τ_4 [ns]	I_4 [%]	τ_5 [ns]	I_5 [%]	τ_{av} [ns]
V1	0.141	10.9	0.527	59.9	1.635	20.6	3.621	6.2	16.893	2.5	1.307
V2	0.155	11.2	0.442	64.8	1.707	14.0	3.504	8.5	20.019	1.4	1.122
V3	0.136	11.3	0.507	56.7	1.423	20.3	2.308	11.2	21.888	0.5	0.953
V4	0.162	11.4	0.476	63.2	1.729	14.4	3.792	9.3	19.046	1.7	1.247
V5	0.139	12.8	0.525	53.8	1.691	24.9	3.339	6.8	16.603	1.7	1.229
V6	0.179	11.6	0.430	67.7	1.703	12.8	3.332	6.7	20.118	1.2	0.987
V7	0.145	12.4	0.518	54.6	1.552	23.2	2.678	8.7	19.435	1.0	1.091
V8	0.157	10.8	0.479	64.8	1.729	14.7	3.861	7.9	18.508	1.8	1.220
R1	0.154	11.4	0.526	61.6	1.723	19.8	4.484	4.4	18.265	2.8	1.395
R2	0.169	10.1	0.427	70.5	1.640	12.3	3.210	6.1	21.234	1.0	0.935
R3	0.180	12.8	0.403	65.6	1.598	12.3	3.153	8.9	15.845	0.4	0.829
R4	0.198	15.2	0.409	63.9	1.658	12.6	3.213	7.8	17.021	0.6	0.845
R5	0.157	12.1	0.535	60.4	1.753	21.5	4.027	3.8	22.765	2.1	1.359